# Structures and Properties of $K_xCr_yNi_{1-x-y}O$ Dielectric Materials Prepared by an Ultrasonic-Assisted Sol-Gel Method

**Bualan Khumpaitool[a]\*** iD**, Songkot Utara[a,b]** iD**, Jinda Khemprasit[c]** iD**, Sujittra Youngme[c]** iD

[a]*Udon Thani Rajabhat University, Faculty of Science, Division of Chemistry, Udon Thani 41000, Thailand*
[b]*Udon Thani Rajabhat University, Faculty of Science, Functional Materials and Composites Research Group, Udon Thani 41000, Thailand*
[c]*Khon Kaen University, Faculty of Science, Materials Chemistry Research Center, Department of Chemistry and Center for Innovation in Chemistry, Khon Kaen 40002, Thailand*

$K_xCr_yNi_{1-x-y}O$ (x = 0.05-0.20, y = 0.02) dielectric materials were prepared using a facile simple green ultrasonic-assisted sol-gel method. All samples have a main phase consisting of a cubic NiO structure and with nanoscale crystallite sizes (28.58-37.51 nm). However, secondary phases were also observed for the samples with x values exceeding 0.10. The fractured surface microstructures of the samples with x values less than 0.15 exhibited uniformly distributed spherical grains. Other samples showed irregularly shaped grains. The grain sizes were larger when x was increased to 0.15 and exhibited increased grain growth probably due to substitution of K ions into the NiO lattice. However, a reduction of grain sizes was observed in the sample with x = 0.20, possibly due to inhibition of the grain growth by the secondary phase. At room temperature and a frequency of 1013 Hz, the highest dielectric constant of $2.25 \times 10^4$ was obtained for the samples with x = 0.15.

**Keywords**: *Ceramics, NiO, Sol-gel process, Dielectric property, Ultrasonic.*

## 1. Introduction

Dielectric materials are lead free and have high dielectric constants. They are attractive for their potential uses in microelectronic device applications such as memory devices and capacitors[1-6]. The search for materials with higher dielectric constants is to enable the reduction of circuit-sizes and to make decisions on the level of miniaturization. Recently, monovalent alkali and transition metal doped NiO systems with the formula, $A_xB_yNi_{1-x-y}O$, have attracted much attention from researchers due to their extraordinarily high dielectric constants[5-8]. As is well-established, NiO is a Mott-Hubbard insulator at room temperature. However, doping with monovalent cations (A) can cause a considerable increase in the electrical conduction of NiO, and thus it becomes a semiconductor due to point defects. Meanwhile, the addition of a transition metal (B) into NiO promotes accumulation of insulating phases at the grain boundaries. Thus, the interior of grains is semiconducting in nature, while the shell of the grains or grain boundaries is an insulator, as one would expect for a boundary layer capacitor (BLC) structure. Many researchers have reportedly tuned the level and types of A (e.g., Li[5,7,9-26], Na[6,27], K[28-31]) and B (e.g., Sn[5], Ti[9,11,13,17,19,24], Si[6,10], Sc[12], Al[14,16], Ta[15], Cr[7,20,21], V[22-24], W[23], Fe[24], Co[25], Cu[26]) additives. Varying their concentration by controlling the A and B additives, Wu and co-workers[9] are the first group to investigate the composition of $Li_xTi_yNi_{1-x-y}O$ (where x ≤ 0.3 and y ≤ 0.1). They report that the optimal compositions of x and y are 0.30 and 0.02, respectively, showing a giant dielectric constant of $10^5$ near

room temperature and weak temperature dependence over a wide temperature range. This huge dielectric constant can be explained using the boundary layer capacitor (BLC) model, consisting of the semiconducting (Li doped NiO) grains and the Ti-rich insulating grain boundaries. Furthermore, some A additives such as Li[9,11,13], Na[6,27] and K[28,29] used for optimizing the concentration of x in $A_xB_yNi_{1-x-y}O$ also exhibit very high dielectric constants (~$10^5$). Among these additives, a K dopant provides for materials with good electrical properties as semiconductors[30] and low solid solubility[32]. Jana's group investigates the addition of K as an A-element, varying the x concentration over the range of 0.04-0.30. The B-element, Ti, is fixed at 0.02 in $K_xTi_yNi_{1-x-y}O$ dielectric materials[28-30]. These materials present interesting results. They have high dielectric constants and low loss tangents with rather weak temperature and frequency dependence. The high dielectric constant of these materials is attributed to the semiconducting grain (K doped NiO) surrounded by Ti-rich insulating grain boundary, as found in BLC model. This behavior is similar to that found for a tuned B addition in doped NiO systems[5,6,21]. In our previous study, we reported the influence of Cr doping on the structure and dielectric properties of $Li_xCr_yNi_{1-x-y}O$ ceramics with varying the concentrations of Cr as 0.02, 0.05 and 0.10 mole[21]. The concentration of Cr dopant is 0.02 mole and has the highest dielectric constant ($\varepsilon_r \sim 10^5$ at room temperature) over a wide frequency range. The huge dielectric constant response observed in this sample may partially result from the microstructure of Li, Cr-doped NiO semiconducting grain surrounded by less conducting (Cr-rich phase) grain boundary, as predicted by BLC structure.

*e-mail: bualan.kh@udru.ac.th

Moreover, a giant dielectric constant may partially result from the high polarization of a large amount of defect dipoles by Cr doping. So far, a report on the structure and dielectric properties of $K_xCr_yNi_{1-x-y}O$ has not been published. Thus, in this work, we have attention to study the dielectric properties of $K_xCr_yNi_{1-x-y}O$ with varying K concentration at levels of 0.05, 0.10, 0.15, and 0.20 mole with a fixed level Cr at 0.02 mole. The purpose of this work is to get the new material having the excellent dielectric properties. The explanation for the high dielectric constants of the NiO-based materials requires several considerations, including increased grain size[28,30], defect dipoles[13,25] and inhomogeneous electrical conduction of semiconducting grains surrounded by more insulating grain boundaries as in a BLCs microstructure[29]. Furthermore, the formation of a huge dielectric constant in these materials depends on the preparation conditions that control the relationship between the structure and properties of the grains and grain boundaries. An ultrasonic-assisted sol-gel method is chosen to prepare $K_xCr_yNi_{1-x-y}O$ in the current research. This is because such a method requires a shorter preparation process compared to the conventional sol-gel process. Furthermore, the ultrasonic method is simple, efficient, green and eco-friendly. Small nanoscale particles[33] and a lower temperature process[34] also resulted. The influence of K doping on the structure and dielectric properties of $K_xCr_yNi_{1-x-y}O$ was also studied.

## 2. Experimental Details

$K_xCr_{0.02}Ni_{0.98-x}O$ materials (x = 0.05-0.20) were prepared via an ultrasonic-assisted sol-gel method. High purity potassium acetate ($CH_3COOK$), nickel (II) acetate tetrahydrate (($CH_3COO)_2Ni \cdot 4H_2O$), and chromium (III) nitrate nonahydrate ($Cr(NO_3)_3 \cdot 9H_2O$) were used as the starting materials with 1,3-propanediol as a chelating agent in the procedure. In this method, stoichiometric amounts of $CH_3COOK$, $(CH_3COO)_2Ni \cdot 4H_2O$ and $Cr(NO_3)_3 \cdot 9H_2O$ were dissolved in deionized water and then mixed with 1,3-propanediol to obtain a precursor solution. A 50 $cm^3$ volume of the precursor solution was placed in a flask (Schlenk Tube, 100 $cm^3$, diameter ($\phi$) 5.0 cm), and its temperature was kept at 25±1 °C by circulating thermostatically-controlled water (0.01 $m^3$) around the flask. The temperature was observed by means of a thermocouple probe (Agilent U1185A; J-Type) immersed in the top half of the solution and connected to a microcomputer. Sonication was carried out for an extended time using a 200 W ultrasonic power supply, a converter and a booster that provided longitudinal vibrations to the horn (diameter ($\phi$) = 0.5 cm) at a frequency of 20 kHz for 1 h[33]. The precursor was dried and calcined in a furnace at 500 °C for 3 h in an air atmosphere with a heating rate of 3 °C/min to obtain an oxide powder. The samples with varying K concentrations are $K_{0.05}Cr_{0.02}Ni_{0.93}O$, $K_{0.10}Cr_{0.02}Ni_{0.88}O$, $K_{0.15}Cr_{0.02}Ni_{0.83}O$ and $K_{0.20}Cr_{0.02}Ni_{0.78}O$. Thermal decomposition of dried samples was examined using TG/DTA (Perkin Elmer, Pyris Diamond) which involved heating to 700 °C at a rate of 10 °C/min under an airflow. The oxide samples were pressed into pellets, 2-3 mm in thickness and then fired at 500 °C for 3 h under an air atmosphere with a heating rate of 3 °C/min. The crystal structure and phase composition of the products were characterized using XRD (PANalytical, EMPYREAN) analysis, employing monochromatic $CuK_\alpha$, with a counting

time of 1.0 sec and scan step of 0.02° from 20° to 80° (2θ). For the phase analysis, the diffractograms of samples were compared with the Crystallography Open Database (COD), using X'Pert HighScore Plus Version 3.0.5 software. The fractured surface morphologies of the pellet samples were characterized using FE-SEM (FEI Helios NanoLab G3 CX). Diffuse reflectance absorption spectra of the samples were recorded on a Shimadzu UV-VIS-NIR3101PC scanning spectrophotometer. The pellet samples were formed into thin plates with smooth surfaces onto which Ag was painted to study their dielectric properties. Their dielectric properties were measured using an impedance analyzer (E4990A, KEYSIGHT) over the frequency range from 100 Hz to 1 MHz.

## 3. Results and Discussion

The TG curve of the $K_{0.15}Cr_{0.02}Ni_{0.83}O$ dried sample (Figure 1) shows three stages of weight loss. The first stage occurs below 150 °C with a small endothermic peak observed at around 70 °C, due to evaporation of residual water in the dried sample[35]. The second stage demonstrates a large weight loss of 36.85% in the TG curve over a temperature range of 150-360 °C, corresponding to a sharp endothermic DTA peak at 345 °C. It may be ascribed to thermal decomposition of residual organics (acetate groups) in the dried sample[17,36]. The final stage yields a 9.30% weight loss over the temperature range of 360-500 °C, accompanied by two exothermic DTA peaks at 390 °C and 500 °C, corresponding to the nucleation and crystallization of oxide products[26,37]. No further weight loss is observed above 500 °C. In this work, the precursors are calcined in air at 500 °C for 3 h, and an oxide phase is obtained at 500 °C as seen in the XRD results.

During synthesis, the black color of pure NiO and doped NiO powders after calcination and sintered pellets is not changed. The XRD patterns of calcined powders (see the supplementary material information for Figure S1) and sintered samples (Figure 2) are found to be similar, which implies that there are no decomposition reactions to produce other phases during the sintering progress[38]. Structural analysis of all samples is refined using the Rietveld technique. The Rietveld refined XRD patterns of pure NiO and the sintered samples with various K concentrations are shown in Figure 2.
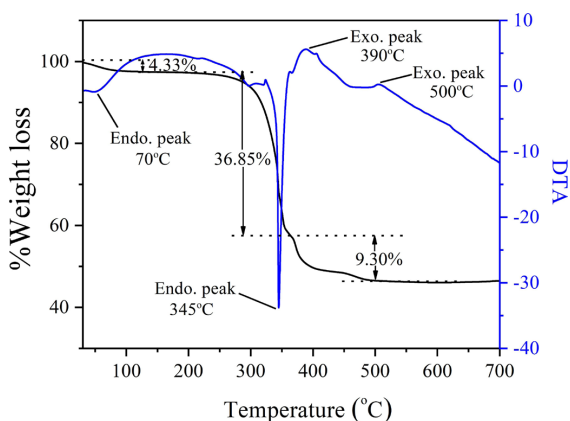


**Figure 1.** TG/DTA curve of the $K_{0.15}Cr_{0.02}Ni_{0.83}O$ sample.

Structures and Properties of K$_x$Cr$_y$Ni$_{1-x-y}$O Dielectric Materials Prepared by an Ultrasonic-Assisted Sol-Gel Method
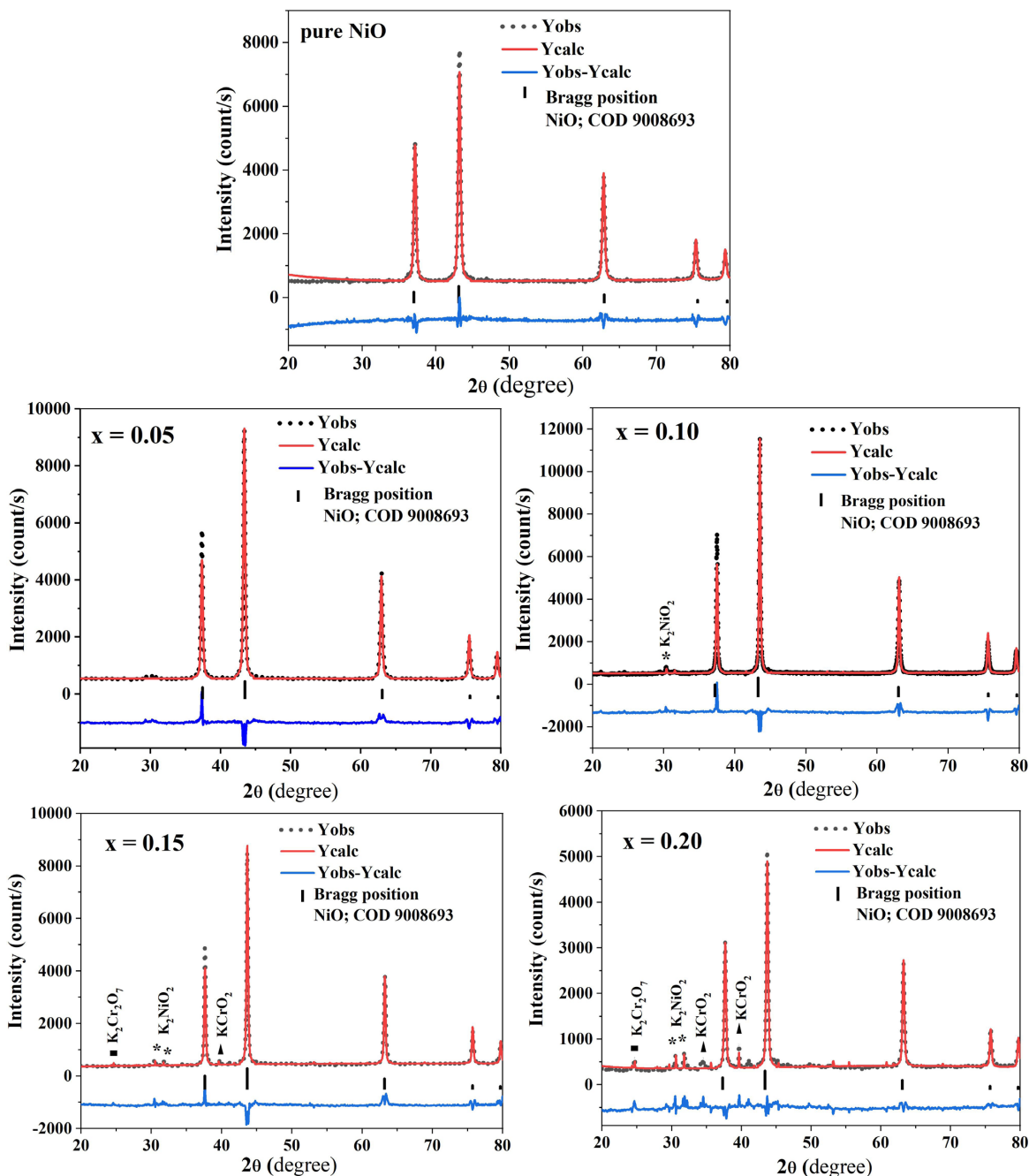
3



**Figure 2.** Rietveld refined parameters of pure NiO and samples with various K concentrations. The dotted symbols represent the observed data points and the red solid line is calculated Rietveld refined data. The vertical black tick marks indicate the position of the Bragg reflections of the cubic NiO phase and the blue solid line at the bottom reveals the difference between the observed data points and the calculated data.

Dotted symbols correspond to the observed data points and the red solid line is the calculated Rietveld result. The vertical black tick marks indicate the position of the Bragg reflections of the cubic NiO phase and the blue solid line at the bottom reveals the difference between the observed data points and the calculated data. It can be seen that all samples could be fitted to the cubic NiO structure within the Fm-3m space group (COD database code: 9008693). All XRD patterns of the cubic NiO structure are nearly identical

and show diffraction peaks at 37.41°, 43.48°, 63.13°, 75.62° and 79.70° that relate to the (111), (002), (022), (113) and (222) planes, respectively. The Rietveld refined parameters and site occupancy of all samples are listed in Table 1. During refinement, the site occupancies of the elements are estimated without constraints. The structural parameters are refined by the Rietveld technique along with the values of the expected weighted profile factor ($R_{exp}$), weighted profile factor ($R_{wp}$) and goodness of fit (GOF) index. It is found that

**Table 1.** The structural refined parameter (a), lattice volume (V), expected weighted profile factor ($R_{exp}$), weighted profile factor ($R_{wp}$), goodness of fit (GOF) and site occupancy of pure NiO and samples with various K contents.

| Parameters | Pure NiO | K concentration | | | |
|---|---|---|---|---|---|
| | | x = 0.05 | x = 0.10 | x = 0.15 | x = 0.20 |
| Lattice parameter (Å) | 4.1768(2) | 4.1787(2) | 4.1806(2) | 4.1827(2) | 4.1839(2) |
| V/ ($10^6$ pm$^3$) | 72.8662 | 72.9687 | 73.0652 | 73.1782 | 73.2381 |
| $R_{exp}$ (%) | 5.28 | 5.32 | 5.36 | 5.88 | 6.42 |
| $R_{wp}$ (%) | 5.76 | 6.70 | 7.83 | 8.50 | 9.59 |
| GOF | 1.19 | 1.58 | 2.14 | 2.09 | 2.23 |
| Site occupancy | | | | | |
| Ni | 1 | 0.930 | 0.880 | 0.830 | 0.780 |
| O | 1 | 1 | 1 | 1 | 1 |
| Cr | | 0.020 | 0.020 | 0.020 | 0.020 |
| K | | 0.050 | 0.100 | 0.150 | 0.200 |

all index parameters can be used as numerical criteria of the quality of fit when calculating the experimental diffraction data, in agreement with other reports[7,39]. The refined lattice parameter values change slightly in comparison with the pure NiO (4.1768 Å) and increase with the K content from 4.1787 to 4.1839 Å, which could possibly result from the larger ionic radius of K$^+$ (1.38 Å) than that of Ni$^{2+}$ (0.69 Å)[40]. All samples show broad diffraction peaks because of their nanocrystalline sizes, which are 28.58, 37.51, 35.60 and 29.72 nm for the samples with x values of 0.05, 0.10, 0.15 and 0.20, respectively. These sizes are determined using Scherrer's formula. Furthermore, small amounts of secondary phases are also observed for some samples, including a $K_2NiO_2$ phase (COD database code: 1530497) in the $K_{0.10}Cr_{0.02}Ni_{0.88}O$ sample, $K_2Cr_2O_7$ (COD database code: 1528259) and $KCrO_2$ (COD database code: 1534559) in the $K_{0.15}Cr_{0.02}Ni_{0.83}O$ and $K_{0.20}Cr_{0.02}Ni_{0.78}O$ samples. The presence of these phases might be due to the remarkable difference between the ionic radii of K$^+$ and Ni$^{2+}$ ions and K content of over 0.10 moles in samples, leading to the limitation of the solid solubility of K$^+$ in the lattice.

FE-SEM images of the samples with various K contents are shown in Figure 3. The fractured surface microstructures of the samples with x values lower than 0.10 reveal uniformly distributed and nearly spherical nano-sizes grains. However, irregularly shaped grains are observed for the samples with K concentrations of 0.15 and 0.20 mole. The grain size distribution of each sample is displayed in their respective histograms. One-hundred grains were counted for each measurement and the average grain sizes ($G_{ave}$) were represented to produce the histograms. It is found that the average grain sizes of all samples are nano-scale and increase with K concentrations from 0.05 to 0.15 mole. There may be some K$^+$ ion substitution into the NiO host lattice that may result from lower activation energy and higher ionic mobility of K$^+$ ion. Thus, the K$^+$ ions enter the nucleation sites and enhance grain growth, leading to increased grain sizes[41]. With a K concentration of 0.20 moles, the average grain size is reduced because of grain growth inhibition in the samples by secondary phases, as reported in other researchers[26,42,43]. The elemental analysis clearly reveals K, Cr, Ni and O components from EDX mapping at 3500× magnification (Figure 4). It can be seen that the K and Cr nanoparticles are well-dispersed throughout the selected
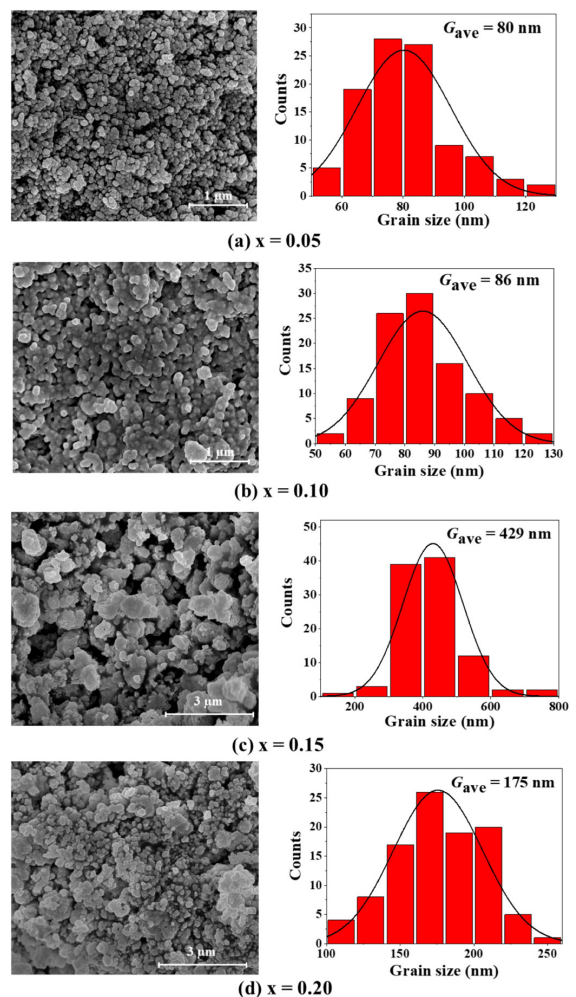


**Figure 3.** Fractured surface morphologies and the corresponding grain size distributions for the $K_xCr_{0.02}Ni_{0.98-x}O$ samples with (a) x = 0.05, (b) x = 0.10, (c) x = 0.15 and (d) x = 0.20.

area in the $K_{0.05}Cr_{0.02}Ni_{0.93}O$ sample (Figure 4a). There is a heterogeneous distribution of K and Cr nanoparticles in the element mapping of the $K_{0.15}Cr_{0.02}Ni_{0.83}O$ sample (Figure 4b), which could have resulted from agglomeration of potassium and chromium oxides as secondary phases. This result is related to the presence of $K_2Cr_2O_7$ and $KCrO_2$ secondary
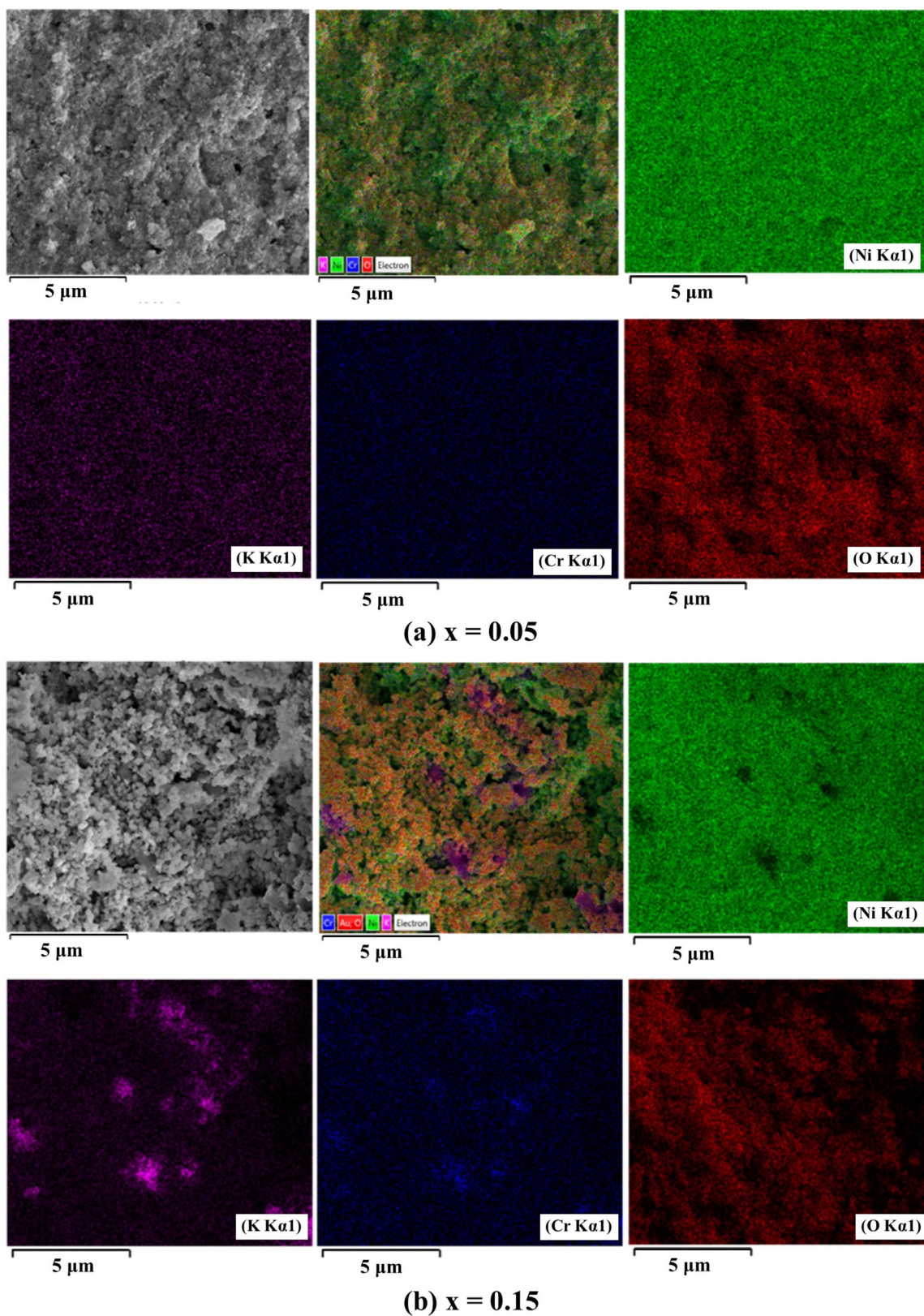
Structures and Properties of K$_x$Cr$_y$Ni$_{1-x-y}$O Dielectric Materials Prepared by an Ultrasonic-Assisted
Sol-Gel Method

5

**(a) x = 0.05**



**(b) x = 0.15**

**Figure 4.** EDX element mapping images of the samples with (a) x = 0.05 and (b) x = 0.15.

phases in the XRD results. The bulk densities of pure NiO and $K_xCr_yNi_{1-x-y}O$ samples with x values of 0.05, 0.10, 0.15, and 0.20 are determined by Archimedes' method as 4.61, 4.63, 3.58, 3.54 and 3.30 g/cm³, respectively. It is found that the bulk density of the sample with an x value of 0.05 is quite close to that of pure NiO and then it decreases rapidly when the K concentration is increased from x = 0.05 to 0.10. However, the bulk density decreases gradually when the K concentration is further increased to x = 0.20. This result is probably explained by the presence of secondary phases in the samples with x values greater than 0.10 (as found in XRD results), leading to inhibition of densification[44,45].

The UV-visible absorption spectra of pure NiO and doped NiO samples are shown in Figure 5a. The absorption edge of pure NiO is 366 nm (3.43 eV), which is in agreement with a previous report[46]. The absorption edges of doped NiO shift to a longer wavelength, which may be due to the formation a narrow band by doping. The optical band gap ($E_g$) can be estimated from a Tauc plot[47] by plotting $(\alpha h\nu)^2$ as a function of photon energy ($h\nu$), as shown in Figure 5b. The optical band energy values for x = 0.05, 0.10, 0.15 and 0.20 are

3.45, 3.26, 3.23 and 3.21 eV, respectively. The reduction in the optical band gap is probably due to the creation of lattice defects such as oxygen vacancies by K doping in NiO. When some of the K+ is substituted for Ni2+ ions, Ni3+ is created as a result of local charge compensation. This leads to formation of oxygen vacancies in the NiO lattice. These oxygen vacancies are probably responsible for the decrease of the optical band gap, which is consistent with the literature[41,47].

The frequency dependence of the dielectric constant ($\varepsilon_r$) and loss tangent (tanδ) at room temperature of the samples with various K concentrations is determined using applied frequencies ranging from 100 Hz to 1 MHz, as displayed in Figure 6. It is found that dielectric constants of the samples with x = 0.05-0.10 are lower with rather weak frequency dependencies. However, those samples with x values greater than 0.15 have very high frequency dependencies at low frequencies and then they decrease steadily as the frequency is increased, due to space charge polarization at low frequencies. These samples exhibit high dielectric constants of about $10^3$-$10^4$ over a wide frequency range of
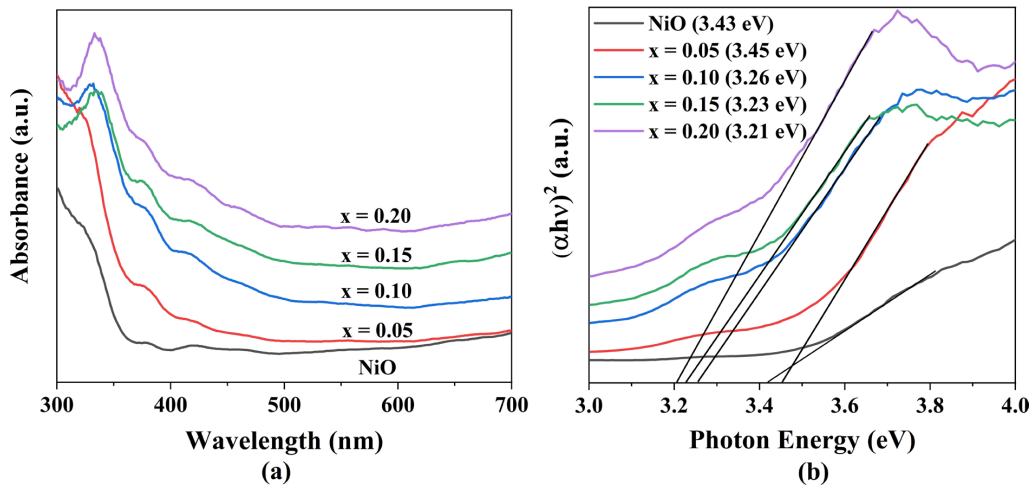


**Figure 5.** (a) Absorption spectra and (b) optical band gap spectra of pure NiO and samples with various K concentrations.
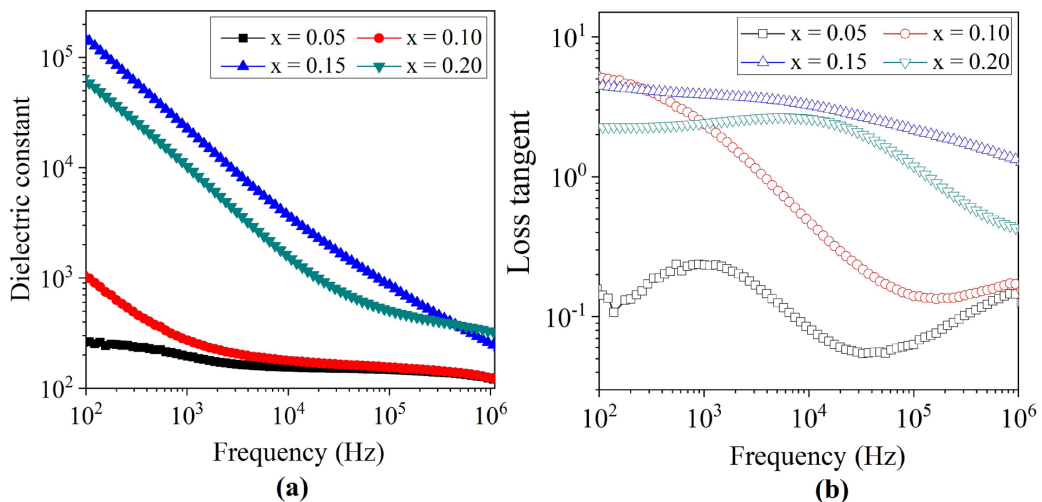


**Figure 6.** Frequency dependence of (a) dielectric constant and (b) loss tangent of the samples with various K contents.

Structures and Properties of $K_xCr_yNi_{1-x-y}O$ Dielectric Materials Prepared by an Ultrasonic-Assisted Sol-Gel Method

7

$10^2$-$10^4$ Hz, which are $10^2$ times higher than that of NiO ($\varepsilon_r$ ~30, at 1 kHz)[13,16]. The dielectric constants tend to increase with K concentrations up to 0.15 mole, which is related to the larger grain sizes. An increase in grain size leads to a greater volume of polarization resulting in a higher dielectric constant, consistent with the published literature[7,27,28,30]. The substitution of a monovalent cation that occurs in $K^+$ doping may generate defect ions and normal oxygen vacancies in the NiO lattice, increasing the electrical conductivity of NiO[32,48]. Thus NiO is semiconducting. The effect of K doping on the dielectric properties in the samples is a key factor because the dopant concentration of Cr is fixed. In addition to the various ion valences, some defects can be introduced by Kröger-Ving notation as follows[49]:

$$K_2O \xrightarrow{NiO} 2K_{Ni}' + V_o^{\cdot\cdot} + O_o^x \tag{1}$$

Defect dipoles are generated by the oxygen vacancy migration. This is related to the UV-visible optical study. Moreover, with the incorporation of $K^+$ into $Ni^{2+}$ ion sites, one neighbouring $Ni^{2+}$ ion transforms into $Ni^{3+}$ due to adjust for charge neutrality[48,49]. $Ni^{2+} \leftrightarrow Ni^{3+}$ transformation leads to electron migration that produces electrical conductivity in the grains. Thus, the defect dipoles ($V_o^{\cdot\cdot}$-$2K_{Ni}'$) and a mixed valence state of $Ni^{2+}$ and $Ni^{3+}$ would increase electrical conductivity of the $K_xCr_{0.02}Ni_{0.98-x}O$ system. With increasing K content, the defect-dipole polarization by $V_o^{\cdot\cdot}$ vacancies increases causing an increase of the total of polarization and more accumulation of charges via conduction in the grain interiors, and hence a larger dielectric constant. At a K content of 0.20 mole, the grain size decreases indicating lower polarization in the grain and a lower dielectric constant[3,45]. The loss tangent values are nearly constant over the measured frequencies for the samples with K concentrations of 0.15 and 0.20 mole, while those of the samples with K concentrations below 0.15 mole depend on the applied frequency. The frequency dependence of tanδ for the samples with K contents of 0.05 and 0.20 shows a tanδ peak, corresponding to a characteristic relaxation process, which is similar to that of $Li_xTi_yNi_{1-x-y}O^9$ and $K_xTi_yNi_{1-x-y}O^{30}$. The relaxation in the frequency of $10^3$-$10^6$ Hz results from interfacial polarization as a Debye-type relaxation. The values of $\varepsilon_r$ and tanδ at 1013 Hz and room temperature for these samples are summarized in Table 2. Among these samples, the one with x = 0.15 provides the best dielectric properties. Its tanδ value is rather independent of the measured frequency. The highest $\varepsilon_r$ ($2.25 \times 10^4$, at 1013 Hz and room temperature) is found for the sample with x = 0.15, which is close to that of (A, B)-doped NiO systems (where A = Li and B = Ti[9,13,18,19], Cr[20], V[22], Fe[24] and Si[10]), calcium copper titanate perovskite materials[4] and slightly higher than that of (Li, Al)-doped NiO[14], (Li, Sn)-doped NiO[5], (K, Ti) doped NiO[31], (Na, Si)-doped NiO[6] and perovskite oxide materials[50]. Its tanδ value is close to that of other NiO-based ceramics such as (Li, Al) doped NiO prepared via a simple thermal decomposition route[14], and (Li, Si)-doped NiO prepared using a chemical precipitation method[10]. However, this value is lower than that of (Li, Cr)-doped NiO[20], (Li, Cu)-doped NiO[26] and (K, Ti)-doped NiO[28].

**Table 2.** Dielectric properties of the samples with various K concentrations.

| K concentration | $\varepsilon_r$ | tanδ |
|---|---|---|
| | at 1013 Hz and room temperature | |
| x = 0.05 | $1.95 \times 10^2$ | 0.23 |
| x = 0.10 | $2.72 \times 10^2$ | 2.37 |
| x = 0.15 | $2.25 \times 10^4$ | 3.84 |
| x = 0.20 | $1.02 \times 10^4$ | 2.42 |

## 4. Conclusions

K and Cr co-doped NiO materials were successfully prepared using an ultrasonic-assisted sol-gel method. The samples with various K contents have a main phase consisting of a cubic NiO structure with nanoscale crystallite sizes. Secondary phases are also observed in the samples with K concentrations of 0.10-0.20 mole. The samples with K concentrations of 0.05-0.10 mole have spherical grains while the other samples exhibit irregularly shaped grains. Moreover, the grain size increases with K concentrations up to 0.15 mole, probably due to incorporation of K ions into the NiO lattice, leading to an enhanced grain size. When K concentrations are increased to level above 0.15 mole, a decreased grain size is obtained, possibly because of inhibition of grain growth by the secondary phases. The dielectric constants of the samples increase with K doping at levels up to 0.15 mole. This is related to their enhanced grain sizes and partial association with the defect dipoles arising from the accumulation of charges via conduction in the grain interior. The $K_{0.15}Cr_{0.02}Ni_{0.83}O$ sample has the best dielectric constant ($2.25 \times 10^4$ at 1013 Hz and room temperature). Moreover, its loss tangent exhibits rather weak frequency dependence.

## 5. Acknowledgements

## 6. References

1. Gao D, Tan Z, Fan Z, Guo M, Hou Z, Chen D, et al. All-inorganic flexible $Ba_{0.67}Sr_{0.33}TiO_3$ thin films with excellent dielectric properties over a wide range of frequencies. ACS Appl Mater Interfaces. 2019;11:27088-97.
2. Mishra AK, Dwibedy D, Devi M, Panigrahi MR. Giant dielectric behaviour of Nb modified CCTO thin film prepared by modified sol-gel route. Transactions on Electrical and Electronic Materials. 2020;21:315-23.
3. Swatsitang E, Putjuso T. Dielectric properties of Ni-doped $Ba_{0.5}Sr_{0.5}TiO_3$ ceramics prepared with hydrothermal synthesized nanopowders. J Sol-Gel Sci Technol. 2014;72:30-6.
4. Boonlakhorn J, Chanlek N, Thongbai P. Giant dielectric permittivity of $CaCu_3Ti_4O_{12}$ via a green solution-egg white method. J Sol-Gel Sci Technol. 2020;93:643-9.

5. Zeng J, He T, Liu Y. Microstructure and electric response of Li,Sn co-doped NiO ceramics. Processing and Application of Ceramics. 2019;13:44-50.

6. Kotb HM, Ahmad MM, Alraheem NA. Study of the structural, impedance spectroscopy and dielectric properties of Na and Si co-doped NiO ceramics. J Phys D Appl Phys. 2017;50:435304.

7. Kumar S, Supriya S, Pradhan KL, Kar M. Effect of microstructure on electrical properties of Li and Cr substituted nickel oxide. J Mater Sci Mater Electron. 2017;28:16679-88.

8. Siddique MN, Ahmed A, Tripathi P. Electric transport and enhanced dielectric permittivity in pure and Al doped NiO nanostructures. J Alloys Compd. 2018;735:516-29.

9. Wu J, Nan CW, Lin Y, Deng Y. Giant dielectric permittivity observed in Li and Ti doped NiO. Phys Rev Lett. 2002;89:217601.

10. Lin Y, Jiang L, Zhao R, Nan CW. High-permittivity core/shell structured NiO-based ceramics and their dielectric response mechanism. Phys Rev B. 2005;72:014103.

11. Mukherjee S, Chatterjee S, Rayaprol S, Bhattacharya S, Jana PK. Near room temperature magnetodielectric consequence in (Li, Ti) doped NiO ceramic. J Appl Phys. 2016;119:134103.

12. Liu Y, Wang W, Huang J, Zhu C, Wang C, Cao Y. High dielectric permittivity of Li and Sc co-doped NiO ceramics. J Mater Sci Mater Electron. 2014;25:1298-302.

13. Lin Y, Zhao R, Wang J, Cai J, Nan CW. Polarization of high-permittivity dielectric NiO-based ceramics. J Am Ceram Soc. 2005;88:1808-11.

14. Tangwancharoen S, Thongbai P, Yamwong T, Maensiri S. Dielectric and electrical properties of giant dielectric (Li, Al)-doped NiO ceramics. Mater Chem Phys. 2009;115:585-9.

15. Hsiao YJ, Chang YS, Fang TH, Chai YL, Chung CY, Chang YH. High dielectric permittivity of Li and Ta codoped NiO ceramics. J Phys D Appl Phys. 2007;40:863-8.

16. Lin Y, Wang J, Jiang L, Chen Y, Nan CW. High permittivity Li and Al doped NiO ceramics. Appl Phys Lett. 2004;85:5664-6.

17. Qureshi A, Mergen A, Altindal A. Preparation and characterization of Li and Ti codoped NiO nanocomposites for gas sensors applications. Sens Actuators B Chem. 2009;135:537-40.

18. Lin YH, Li M, Nan CW, Li J, Wu J, He J. Grain and grain boundary effects in high-permittivity dielectric NiO-based ceramics. Appl Phys Lett. 2006;89:032907.

19. Thongbai P, Yamwong T, Maensiri S. The sintering temperature effects on the electrical and dielectric properties of $Li_{0.05}Ti_{0.02}Ni_{0.93}O$ ceramics prepared by a direct thermal decomposition method. J Appl Phys. 2008;104:074109.

20. Khumpaitool B, Khemprasit J. Effect of calcining temperature on structural and dielectric properties of $Li_{0.30}Cr_{0.02}Ni_{0.68}O$ ceramics. J Alloys Compd. 2014;587:211-6.

21. Khemprasit J, Khumpaitool B. Influence of Cr doping on structure and dielectric properties of $Li_xCr_yNi_{1-x-y}O$ ceramics. Ceram Int. 2015;41:663-9.

22. Pongha S, Thongbai P, Yamwong T, Maensiri S. Giant dielectric response and polarization relaxation mechanism in (Li, V)-doped NiO ceramics. Scr Mater. 2009;60:870-3.

23. Chen GJ, Hsiao YJ, Chang YS, Chai YL. Structure and high dielectric permittivity of $Li_{0.01}M_{0.05}Ni_{0.94}O$ (M = V and W) ceramics. J Alloys Compd. 2009;474:237-40.

24. Thongbai P, Pongha S, Yamwong T, Maensiri S. Effects of Fe, Ti, and V doping on the microstructure and electrical properties of grain and grain boundary of giant dielectric NiO-based ceramics. Appl Phys Lett. 2009;94:022908.

25. Li Y, Fang L, Liu L, Huang Y, Hu C. Giant dielectric response and charge compensation of Li- and Co-doped NiO ceramics. Mater Sci Eng B. 2012;177:673-7.

26. Xu D, He K, Chen BH, Jiao L, Wu W, Mu S, et al. Dielectric and varistor properties of Cu doped $Li_{0.02}Ni_{0.98}O$ ceramics. J Mater Sci Mater Electron. 2015;26:9831-6.

27. Jana PK, Sarkar S, Sakata H, Watanabe T, Chaudhuri BK. Microstructure and dielectric properties of $Na_xTi_yNi_{1-x-y}O$ (x = 0.05-0.30, y = 0.02). J Phys D Appl Phys. 2008;41:065403.

28. Jana PK, Sarkar S, Chaudhuri BK. Low loss giant dielectric and electrical transport behavior of $K_xTi_yNi_{1-x-y}O$. Appl Phys Lett. 2006;88:82901.

29. Jana PK, Sarkar S, Chaudhuri BK. Effects of K doping and annealing on the grain size and giant dielectric constant of $K_xTi_{0.02}Ni_{0.98-x}O$ ceramics. Phys Status Solidi, A Appl Mater Sci. 2007;204:1580-8.

30. Jana PK, Sarkar S, Karmakar S, Chaudhuri BK. Conduction mechanism and dielectric relaxation in high dielectric $K_xTi_yNi_{1-x-y}O$. J Appl Phys. 2007;102:084105.

31. Cheng B, Lin YH, Mei A, Cai JN, Nan CW, He J. Effects of grain modification on the dielectric properties of $A_{0.03}Ti_{0.10}Ni_{0.87}O$ (A: $K^+$, $Mg^{2+}$, $Y^{3+}$) ceramics. Appl Phys Lett. 2008;92:142903.

32. Loukil A, Boukhachem A, Amor MB, Ghamnia M, Raouadi K. Effects of potassium incorporation on the structural, optical, vibrational and electrical properties of NiO sprayed thin films for p-type optical windows. Ceram Int. 2016;42:8274-89.

33. Utara S, Klinkaewnarong J. Sonochemical synthesis of nano-hydroxyapatite using natural rubber latex as a templating agent. Ceram Int. 2015;41:14860-7.

34. Ghows N, Entezari MH. Ultrasonic with low intensity assisted the synthesis of nanocrystalline $TiO_2$ without calcination. Ultrason Sonochem. 2010;17:878-83.

35. Al Boukhari J, Khalaf A, Awad R. Structural and electrical investigations of pure and rare earth (Er and Pr)-doped NiO nanoparticles. Appl Phys, A Mater Sci Process. 2020;126:74.

36. De Jesúsa JC, González I. Preparation of nickel nanoparticles and their catalytic activity in the cracking of methane. J Vac Sci Technol A. 2008;26:913-8.

37. Khemprasit J, Kaen-ngam S, Khumpaitool B, Kamkhou P. Effects of calcining temperature on structural and magnetic properties of nanosized Fe-doped NiO prepared by diol-based sol-gel process. J Magn Magn Mater. 2011;323:2408-12.

38. Luo T, He L, Yang H, Yu H. Phase evolution and microwave dielectric properties of $BaTi_4O_9$ ceramics prepared by reaction sintering method. Int J Appl Ceram Technol. 2019;16:146-51.

39. Dara MA, Varshney D. Structures and properties of $Mg_{0.95}Mn_{0.01}TM_{0.04}O$ (TM = Co, Ni, and Cu) nanoparticles synthesized by sol-gel auto combustion technique. RSC Advances. 2018;8:14120-8.

40. Wang N, Liu CQ, Liu B, Wen CQ, Wen B, Wang HL, et al. Structural, electrical and optical properties of K-doped NiO films prepared by rapid pyrolysis sol-gel technique. Thin Solid Films. 2016;616:587-93.

41. Bhatt AS, Ranjitha R, Santosh MS, Ravikumar CR, Prashantha SC, Maphanga RR, et al. Optical and electrochemical applications of Li-doped NiO nanostructures synthesized via facile microwave technique. Materials (Basel). 2020;13:2961.

42. Lakshmi SN, Chandran D, Anandakumar VM, Rajendra Babu KN. Structure and room-temperature ferrromagnetism evolution of Sn and Mn-doped NiO synthesized by a sol-gel process. Ceram Int. 2017;43:11090-6.

43. Cheng X, Wang Y, Chen X, Cui H. Investigation on electrical properties and microdefects of $Nb^{5+}$-doped $BaTiO_3$ based ceramics by positron annihilation techniques. Mater Res. 2019;22(Suppl 2):e20180921.

44. Tekeli S, Gürü M, Sağlam OE. Densification and grain-growth behavior of various amounts of $SiO_2$ doped 8YSCZ/$SiO_2$ composites. Mater Manuf Process. 2007;22:710-4.

45. Tzing WH, Tuan WH, Lin HL. The effect of microstructure on the electrical properties of NiO-doped $BaTiO_3$. Ceram Int. 1999;25:425-30.

46. Al Boukhari J, Zeidan L, Khalaf A, Awad R. Synthesis, characterization, optical and magnetic properties of pure and Mn, Fe and Zn doped NiO nanoparticles. Chem Phys. 2019;516:116-24.

Structures and Properties of $K_xCr_yNi_{1-x-y}O$ Dielectric Materials Prepared by an Ultrasonic-Assisted Sol-Gel Method

9

47. Sharma R, Yadav K. Effect of lattice defects on the structural and optical properties of $Ni_{1-x}Ag_xO$ (where x = 0.0, 0.01, 0.03, 0.05, 0.10 and 0.15) nanoparticles. Appl Phys, A Mater Sci Process. 2018;124:88.

48. Yang M, Pu H, Zhou Q, Zhang Q. Transparent p-type conducting K-doped NiO films deposited by pulsed plasma deposition. Thin Solid Films. 2012;520:5884-8.

49. Yin X, Han J, Zhou Y, Gu Y, Tai M, Nan H, et al. Critical roles of potassium in charge-carrier balance and diffusion induced defect passivation for efficient inverted perovskite solar cells. J Mater Chem A Mater Energy Sustain. 2019;7:5666-76.

50. Caceres JAS, Passos CAC, Chagas JVS, Barbieri RC, Corteletti RT. Study of structural and electric properties of the PZT 52/48 doped with $Er^{+3}$. Mater Res. 2019;22(5):e20190123.

## Supplementary material

The following online material is available for this article:

Figure S1 - XRD patterns of pure NiO and sample powders with various K contents after calcination.

This material is available as part of the online article from http://www.scielo.br/MR